




Article

# The Origin of Synergetic Effect in Mixed Mn-Co Oxide with Spinel Structure for Catalytic Oxidation of CO

Olga A. Bulavchenko <sup>1,2,\*</sup> , Vladimir A. Rogov <sup>2</sup>, Evgeny Yu. Gerasimov <sup>2</sup> , Egor E. Aydakov <sup>1</sup> and Anna M. Kremneva <sup>1</sup> 

<sup>1</sup> Synchrotron Radiation Facility SKIF, Nikolsky Prosp., 1, 630559 Kol'tsovo, Russia

<sup>2</sup> Physical Department, Novosibirsk State University, Pirogova 2, 630090 Novosibirsk, Russia

\* Correspondence: isizy@mail.ru

**Abstract:** In this work, the origin of the synergetic effect in mixed  $Mn_xCo_{3-x}O_4$  oxides with the spinel structure in the CO oxidation reaction was tested. A series of  $Mn_xCo_{3-x}$  oxide catalysts were synthesized by the coprecipitation method with further calcination at 600 °C and varying manganese content from  $x = 0$  to  $x = 3$ . The catalysts were characterized using XRD, TEM,  $N_2$  adsorption, TPR, EXAFS, and XPS. The catalytic activity of  $Mn_xCo_{3-x}$  oxide catalysts was tested in CO oxidation reactions. The addition of manganese to cobalt oxide results in the formation of mixed Mn-Co oxides based on a cubic or tetragonal spinel structure, a change in microstructural properties, such as surface area and crystal size, as well as local distortions and a decrease in the surface concentration of Co ions and Co in the octahedral sites in spinel structure; it also decreases catalyst reducibility. For all catalysts, the activity of CO oxidation decreases as follows:  $Mn_{0.1}Co_{2.9} > Co_3O_4 \sim Mn_{0.3}Co_{2.7} > Mn_{0.5}Co_{2.5} > MnO_x > Mn_{0.7}Co_{2.3} > Mn_{0.9}Co_{2.1} \sim Mn_{1.1}Co_{1.9} \sim Mn_{2.5}Co_{0.5} > Mn_{2.9}Co_{0.1} > Mn_{1.7}Co_{1.3} > Mn_{2.1}Co_{0.9} > Mn_{1.3}Co_{1.7} \sim Mn_{1.5}Co_{1.5} \sim Mn_{2.3}Co_{0.7}$ . The  $Mn_{0.1}Co_{2.9}$  catalyst displays the best catalytic activity, which is attributed to its small crystal size and the maximum surface ratio between  $Co^{3+}$  and  $Co^{2+}$ . A further increase in the manganese content ( $x > 0.3$ ) provokes drastic changes in the catalytic properties due to a decrease in the cobalt content on the surface and in the volume of mixed oxide, changes in the oxidation states of cations, and structure transformation.



Academic Editors: Tobias Krämer and Geun-Ho Han

Received: 27 November 2024

Revised: 27 December 2024

Accepted: 29 December 2024

Published: 31 December 2024

**Citation:** Bulavchenko, O.A.; Rogov, V.A.; Gerasimov, E.Y.; Aydakov, E.E.; Kremneva, A.M. The Origin of Synergetic Effect in Mixed Mn-Co Oxide with Spinel Structure for Catalytic Oxidation of CO. *Inorganics* **2025**, *13*, 8. <https://doi.org/10.3390/inorganics13010008>

**Copyright:** © 2024 by the authors. Licensee MDPI, Basel, Switzerland. This article is an open access article distributed under the terms and conditions of the Creative Commons Attribution (CC BY) license (<https://creativecommons.org/licenses/by/4.0/>).

**Keywords:**  $Mn_xCo_{3-x}O_4$  oxides; solid solutions; synergetic effect; CO oxidation

## 1. Introduction

Transition metal oxide catalysts ( $Co_3O_4$ , CuO,  $Mn_3O_4$ ,  $Cr_2O_3$ ,  $Fe_2O_3$ , etc.) attract attention as promising catalysts for the oxidation of CO, hydrocarbons, and volatile organic compounds [1,2]. They are expected to be a better alternative to replace the noble metal catalysts since transition metal oxides are cheaper, resistant to poisons, and have good redox ability and flexible valence states. However, single-oxide catalysts usually have moderate activity in oxidation reactions. One approach to improve catalytic performance is to combine two or more metal elements, which usually exhibit superior catalytic activity as compared to the arithmetic summation of individual oxides due to the synergetic effect [3,4]. The synergetic effect results in an enhancement or improvement in catalytic performance. Its origin can be both in the different roles of the components in activity, stability, and selectivity and in changes in electronic, structural, and microstructural properties [3].

Cooperation between Mn and Co is of interest since these oxides have their own activity [1] and tend to interact with each other in the formation of solid solutions and new

compounds [5]. Many authors have noted a synergetic effect in the improved catalytic properties of VOCs [6–11] and CO oxidation [12,13] for MnCoO<sub>x</sub> oxide catalysts. Aguilera et al. found that the catalytic behavior during the oxidation of toluene, ethanol, and butanol in mixed MnCoO<sub>x</sub> oxide catalysts differs from that observed in catalysts containing only manganese as an active phase [9]. This difference was attributed to the beneficial impact of metal interactions, which enhance the oxide reducibility, leading to the formation of amorphous phases and thus increasing the catalytic activity in oxidation reactions. Among the Co/Mn/Mg/Al mixed oxide catalysts obtained by the thermal decomposition of hydrotalcite with a variation in the Mn/(Co + Mn) ratio from 0 to 0.67, the catalyst with Mn/(Co + Mn) = 0.67 showed the highest activity in toluene oxidation [9]. Tang et al. found that the formation of a Mn<sub>x</sub>Co<sub>3-x</sub>O<sub>4</sub> (Mn/(Co + Mn) = 0.5) solid solution with a spinel structure and a high surface area leads to an increase in the VOC oxidation reaction due to the strong synergetic effect of Mn and Co in the oxide and the low-temperature reducibility [7]. The following work by the authors of [10] was devoted to investigating the effect of the Mn/(Co + Mn) ratio from 0.1 to 10; the catalyst with a Mn/(Co + Mn) ratio of 0.5 showed the best activity for benzene conversion. Faure et al. used the controlled decomposition of oxalates to produce mixed oxides of Mn<sub>x</sub>Co<sub>3-x</sub>O<sub>4</sub> with a spinel structure and a very large surface area [12]. These spinel oxides exhibit an outstanding catalytic activity for propane and CO oxidation. The authors found that the high activity is correlated both with the surface area and the cobalt concentration. With an increasing Co content, an almost linear dependence was observed; the most efficient catalyst was Co<sub>2.3</sub>Mn<sub>0.7</sub>O<sub>4</sub> [12]. Liu et al. investigated mesoporous Mn-doped Co<sub>3</sub>O<sub>4</sub> catalysts prepared via a dry soft reactive grinding method with further calcination at 300 °C and tested their catalytic performances in CO oxidation. A significant promotion effect was observed when the atomic ratios of Mn/(Co + Mn) were lower than 0.1. For all the samples, the descending order of activity of Mn/(Co + Mn) was as follows: 0.05~0.1 > 0 (Co<sub>3</sub>O<sub>4</sub>) > 0.2 > 0.3 > 1 (MnO<sub>x</sub>) [13]. Zhang et al. tested a series of catalysts with different Mn/(Mn + Co) molar ratios in the catalytic combustion of benzene [6]. The MnCoO<sub>x</sub> catalyst with Mn/(Mn + Co) = 0.5 exhibited the best activity compared with other cation ratios of 0.5–0.15, as well as single Co<sub>3</sub>O<sub>4</sub> and MnO<sub>x</sub> [6].

As can be seen from the literature, there is a contradiction in the composition of active catalysts (the optimal Mn/(Co + Mn) ratio varies from 0.05 to 0.67) [6,9,10,12,13]. Within a similar chemical composition, the state of the active catalyst varies and depends on the method of synthesis and the mechanism of the catalytic reaction. Several works emphasize the role of the presence of a Mn<sub>x</sub>Co<sub>3-x</sub>O<sub>4</sub> oxide with a spinel structure [7,10,12]. Generally, the most active catalysts were prepared at relatively low temperatures of 300–400 °C, which may lead to the formation of dispersed and difficult-to-detect active states. For example, in the case of a Mn<sub>5</sub>Co<sub>1</sub>O<sub>x</sub> catalyst prepared at 400 °C, the formation of CoMnO<sub>3</sub> nanoparticles was detected [14]. During the decomposition of an oxalate precursor at temperatures up to 300 °C, oxides such as MnO<sub>1.6</sub> and Mn<sub>5</sub>O<sub>8</sub> can be found [15–17].

To the best of our knowledge, no systematic studies concerning the effect of spinel composition in the wide range of manganese content on catalytic properties have been conducted. The purpose of this work is to investigate the origin of the synergetic effect in the case of Mn<sub>x</sub>Co<sub>3-x</sub>O<sub>4</sub> oxides, depending on the cation content. Herein, we used a relatively high calcination temperature of 600 °C in order to eliminate the influence of highly dispersed states. X-ray diffraction (XRD), transmission electron microscopy (TEM), N<sub>2</sub> adsorption, X-ray absorption fine structure (EXAFS), temperature-programmed reduction in hydrogen (TPR-H<sub>2</sub>), and X-ray photoelectron spectroscopy (XPS) techniques were used to study the structure as well as the redox and surface properties of the catalysts. Catalytic properties were tested in a CO oxidation reaction.

## 2. Results

### 2.1. Catalytic Activity

Figure 1a shows the evolution of CO conversion as a function of temperature for the  $Mn_xCo_{3-x}$  catalysts. Figure 1b illustrates the temperature of 50% conversion of CO ( $T_{50}$ ) depending on the Mn content ( $x$ ). For the pure cobalt oxide catalyst ( $Mn_0Co_3$ ,  $x = 0$ ), the temperature of 50% conversion was 129 °C. The addition of Mn up to  $x = 0.1$  led to a shift of the light-off curve to a low-temperature region, and  $T_{50}$  decreased to 97 °C. Further introduction of Mn ions led to the opposite effect: the CO conversion curves shifted from  $x = 0.3$  to 3 to a higher temperature region, and  $T_{50}$  changed from 130 ( $x = 0.3$ ) to 280 °C ( $x = 1.9$ ). For all the samples, the  $T_{50}$  value increased in the following sequence:  $Mn_{0.1}Co_{2.9} < Co_3O_4 \sim Mn_{0.3}Co_{2.7} < Mn_{0.5}Co_{2.5} < MnO_x < Mn_{0.7}Co_{2.3} < Mn_{0.9}Co_{2.1} \sim Mn_{1.1}Co_{1.9} \sim Mn_{2.5}Co_{0.5} < Mn_{2.9}Co_{0.1} < Mn_{1.7}Co_{1.3} < Mn_{2.1}Co_{0.9} < Mn_{1.3}Co_{1.7} \sim Mn_{1.5}Co_{1.5} \sim Mn_{2.3}Co_{0.7}$ . It is worth noting that 50% CO conversion of the  $Mn_3Co_0$  ( $x = 3$ ) catalyst was achieved at 221 °C. In the range of  $x$  from 2.9 to 0.7, a noticeable shift of the CO conversion curve to a higher temperature region was observed, and  $T_{50}$  changed from 221 to 280 °C. This indicates that the addition of Co ions to manganese oxide provokes a negative effect on the catalytic activity. To elucidate the nature of active components, we will further investigate the properties of the catalysts by physicochemical methods.

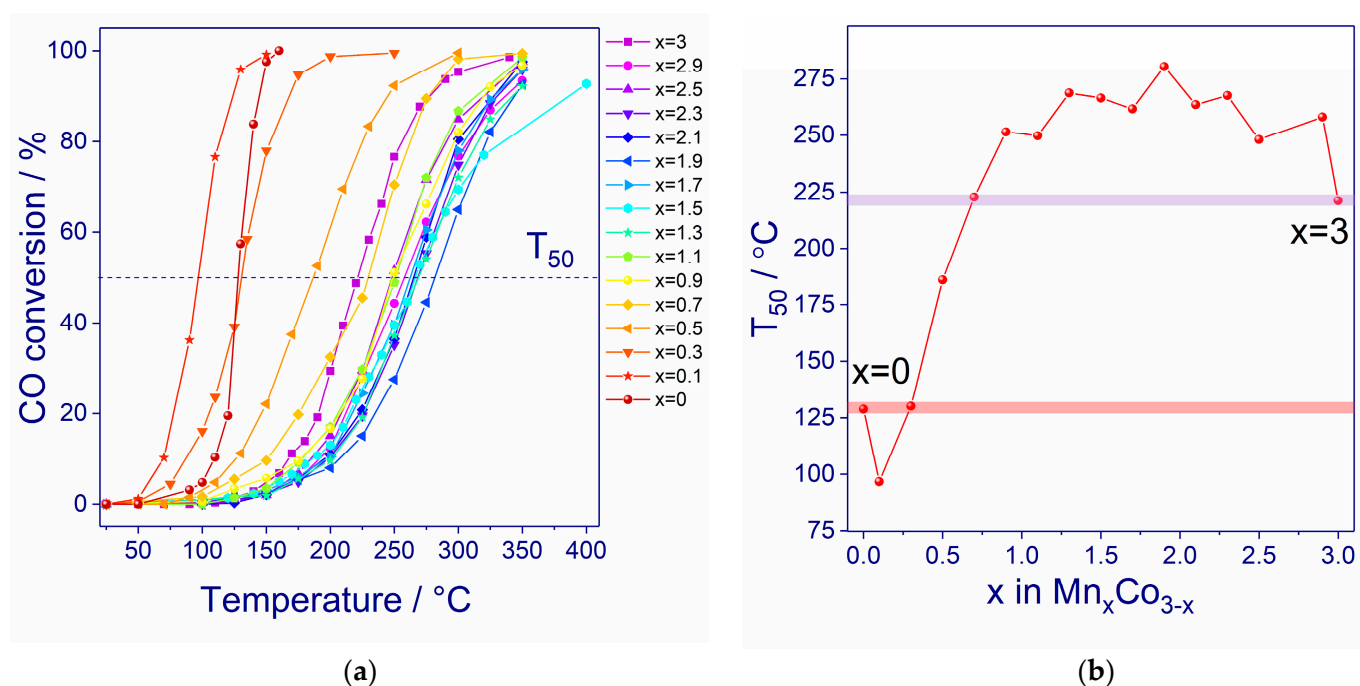


**Figure 1.** Reaction temperature dependence of CO oxidation conversion (a) and temperature of 50% CO conversion depending on the manganese content ( $x$ ) in  $Mn_xCo_{3-x}$  catalysts (b).

### 2.2. Structural and Microstructural Properties

Figure 2 shows X-ray diffraction patterns for  $Mn_xCo_{3-x}$  with  $x = 0, 0.1, 0.3, 0.5, 0.7, 1.1, 1.9, 2.5,$  and 3. For  $x = 0$ , the XRD pattern contained diffraction peaks at  $2\theta = 8.7, 14.2, 16.6, 17.4, 20.2, 24.8, 26.4,$  and  $28.7^\circ$ , corresponding to 111, 220, 311, 222, 400, 422, 511, and 440 reflections of  $Co_3O_4$  with a cubic spinel structure (space group  $Fd\bar{3}m$ , PDF No. 431003). With an increase in  $x$  from 0 to 1.1, the broadening of the diffraction reflections and their shift towards low angles took place. The appearance of other diffraction reflections was not observed. Table 1 summarizes the phase composition, lattice parameters, crystal size, and strains calculated using the Rietveld refinement. The introduction of Mn into cobalt oxide led to an increase in the lattice parameters from 8.084(2) to 8.191(1) Å. The

ionic radius of Mn was larger than that of Co ( $\text{Mn}^{3+} - r = 0.58 \text{ \AA}$ ,  $\text{Co}^{3+} - r = 0.55 \text{ \AA}$ , for coordination number of 6;  $\text{Mn}^{2+} - r = 0.66 \text{ \AA}$ ,  $\text{Co}^{3+} - r = 0.56 \text{ \AA}$ , for coordination number of 4 [18]); the increase in the lattice parameter indicated the incorporation of manganese into the oxide structure with the formation of  $\text{Mn}_x\text{Co}_{3-x}\text{O}_4$  solid solutions based on the cubic spinel structure. Simultaneously, the crystal size changed from 550(70) to 120(10)  $\text{\AA}$ , the strains from 0.14(2) to 0.36(2) %, and the specific surface area increased from 25 to 44  $\text{m}^2/\text{g}$ . During the formation of solid solutions, an increase in strains was observed due to the difference in the atomic radii of the elements. Geometrically, different atoms are located at crystallographically equivalent positions, leading to local distortions and deformations. Moreover, the octahedrally coordinated  $\text{Mn}^{3+}$  is a Jahn–Teller ion. It is in a degenerate electronic state and undergoes a tetragonal Jahn–Teller distortion that lowers the symmetry of the octahedral. This increase in stress leads to a loss of long-range order in the arrangement of atoms and, consequently, a decrease in the crystal size.

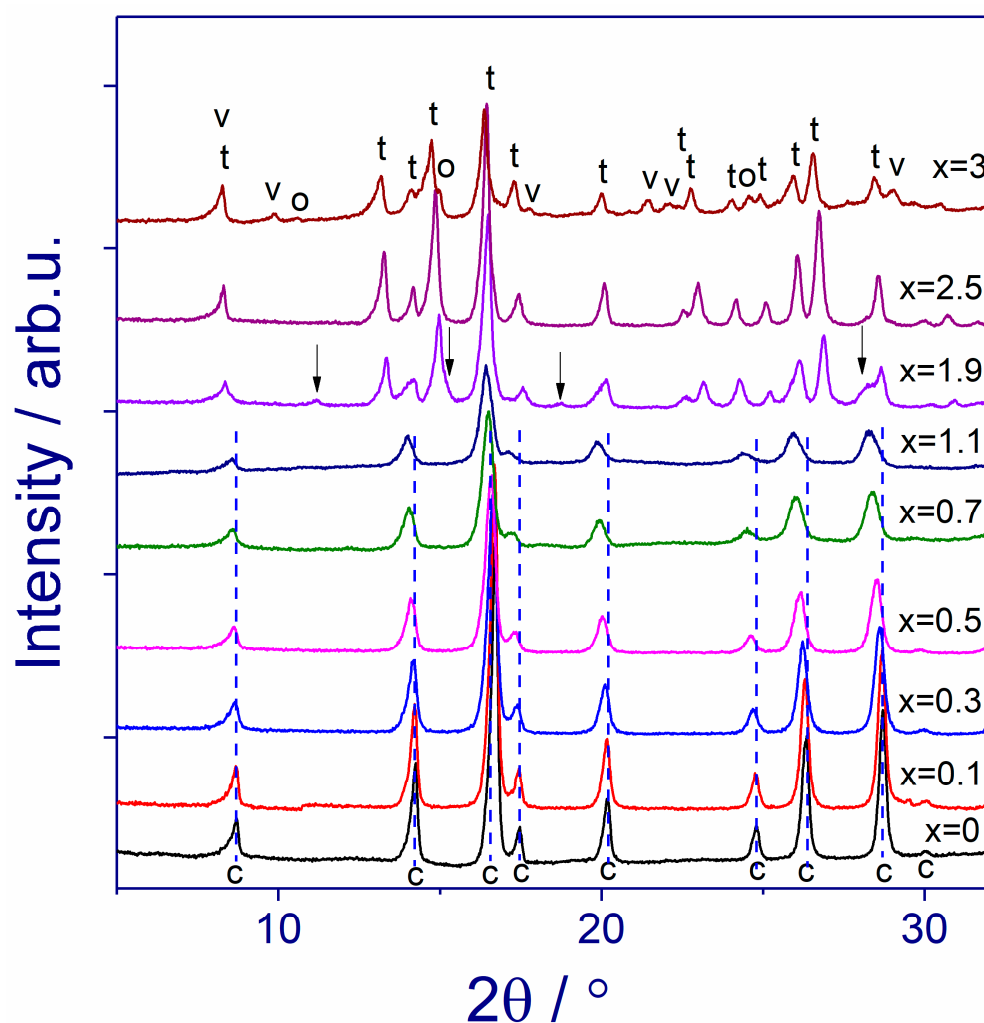


**Figure 2.** XRD patterns ( $\text{MoK}_{\alpha 1}$  radiation) for the  $\text{Mn}_x\text{Co}_{3-x}$  catalysts ( $x = 0, 0.1, 0.3, 0.4, 0.7, 1.1, 1.9, 2.5, 3$ ). Dot lines show the position of the  $\text{Co}_3\text{O}_4$  ( $\text{Mn}_x\text{Co}_{3-x}$ ,  $x = 0$ ) reflections. Symbols c indicate the  $\text{Mn}_x\text{Co}_{3-x}\text{O}_4$  cubic spinel reflections, t—the  $\text{Mn}_x\text{Co}_{3-x}\text{O}_4$  tetragonal spinel reflections, o— $\text{Mn}_2\text{O}_3$ , v— $\text{Mn}_5\text{O}_8$ , and the asterisks— $\text{CoMnO}_3$ .

**Table 1.** Phase composition, lattice parameters, crystal size, strains ( $\epsilon_0$ ) according to Rietveld refinement, and specific surface area (S) for the  $Mn_xCo_{3-x}$  catalysts.

Catalysts	Phase Composition, wt %	Lattice Parameter, Å	Crystal Size, Å	$\epsilon_0$ , %	S, m <sup>2</sup> /g
Co <sub>3</sub> O <sub>4</sub>	100% Co <sub>3</sub> O <sub>4</sub> (cubic)	8.084 (2)	550 (70)	0.14 (2)	25
Mn <sub>0.1</sub> Co <sub>2.9</sub>	100% Mn <sub>x</sub> Co <sub>3-x</sub> O <sub>4</sub> (cubic)	8.092 (1)	220 (10)	0.12 (1)	26
Mn <sub>0.3</sub> Co <sub>2.7</sub>	100% Mn <sub>x</sub> Co <sub>3-x</sub> O <sub>4</sub> (cubic)	8.104 (1)	160 (10)	0.17 (2)	27
Mn <sub>0.5</sub> Co <sub>2.5</sub>	100% Mn <sub>x</sub> Co <sub>3-x</sub> O <sub>4</sub> (cubic)	8.113 (1)	170 (20)	0.26 (2)	29
Mn <sub>0.7</sub> Co <sub>2.3</sub>	100% Mn <sub>x</sub> Co <sub>3-x</sub> O <sub>4</sub> (cubic)	8.154 (1)	140 (10)	0.35 (2)	46
Mn <sub>1.1</sub> Co <sub>1.9</sub>	100% Mn <sub>x</sub> Co <sub>3-x</sub> O <sub>4</sub> (cubic)	8.191 (1)	120 (10)	0.36 (2)	44
Mn <sub>1.9</sub> Co <sub>1.1</sub>	96% Mn <sub>x</sub> Co <sub>3-x</sub> O <sub>4</sub> (tetragonal)	5.730 (1)	240 (60)	0.17 (2)	48
	4% CoMnO <sub>3</sub>	9.260(2)	230 (50)	-	
Mn <sub>2.5</sub> Co <sub>0.5</sub>	100% Mn <sub>x</sub> Co <sub>3-x</sub> O <sub>4</sub> (tetragonal)	5.741 (1)	260 (10)	0.10(1)	21
		9.341 (1)			
MnO <sub>x</sub>	55% Mn <sub>3</sub> O <sub>4</sub>	-	250 (30)	-	21
	35% Mn <sub>5</sub> O <sub>8</sub>		80 (10)		
	10% Mn <sub>2</sub> O <sub>3</sub>		250 (20)		

For  $x = 1.9$  and  $2.5$ , the diffraction pattern drastically changed. The XRD peaks at  $2\theta = 8.3, 13.3, 14.1, 15.0, 16.4, 17.4, 20.0, 22.5, 23.0, 24.1, 25.1, 26.1, 26.7,$  and  $28.6^\circ$ , which belong to the tetragonal spinel of the Mn<sub>3</sub>O<sub>4</sub> type (space group  $I4_1/amd$ , PDF No. 240734), were observed (Figure 2). With an increase in the concentration of manganese from  $x = 1.1$  to  $x = 1.9$ , a phase transition from the cubic to the tetrahedral modification occurred due to the cooperative Jahn–Teller effect. The observed lattice parameters were smaller than those for pure Mn<sub>3</sub>O<sub>4</sub> ( $a = b = 5.762$  Å,  $c = 9.469$  Å, PDF No. 240734), indicating the incorporation of Co ions into the structure of manganese oxide (Table 1). In the case of the Mn<sub>1.9</sub>Co<sub>1.1</sub> catalyst, the XRD pattern contained additional peaks at  $2\theta = 11.2, 18.7,$  and  $27.1^\circ$  due to the appearance of the CoMnO<sub>3</sub> oxide (PDF No. 120476). The XRD pattern of MnO<sub>x</sub> ( $x = 3$ ) significantly differed from the previous samples. It contained reflections of Mn<sub>5</sub>O<sub>8</sub> ( $2\theta = 8.3, 9.9, 17.7, 21.4, 22.0,$  and  $29.0^\circ$ , PDF No. 391218), Mn<sub>3</sub>O<sub>4</sub> (PDF No. 240734), and Mn<sub>2</sub>O<sub>3</sub> ( $2\theta = 10.7, 15.0,$  and  $24.6^\circ$ , PDF No. 411442). Estimation of the phase composition showed that the sample contained 55 wt % Mn<sub>3</sub>O<sub>4</sub>, 35 wt % Mn<sub>5</sub>O<sub>8</sub>, and 10 wt % Mn<sub>2</sub>O<sub>3</sub>. It is worth noting that the introduction of even a small amount of cobalt (17 at%) stabilized the spinel structure, which is consistent with the phase diagram for the Mn–Co–O system [5].

TEM images of the Co<sub>3</sub>O<sub>4</sub> and Co<sub>0.1</sub>Mn<sub>2.9</sub> catalysts are presented in Figure 3. The Co<sub>3</sub>O<sub>4</sub> consisted of round-shaped and plate-shaped particles with sizes of about 25–60 nm (Figure 3a). In the case of the Mn<sub>0.1</sub>Co<sub>2.9</sub>, the particles were smaller; particles with sizes of about 20–30 nm were observed. EDS mapping showed a predominantly uniform distribution of Co and Mn over the sample volume (Figure 3c,d); the ratio between Mn and Co was 0.03. Figure 3e demonstrates the crystalline structure of Co<sub>3</sub>O<sub>4</sub> well. For the Mn<sub>0.1</sub>Co<sub>2.9</sub> catalyst, the crystal structure contained defects; Figure 3f shows the micro strains, and arrows indicate micro strains in the FT image.

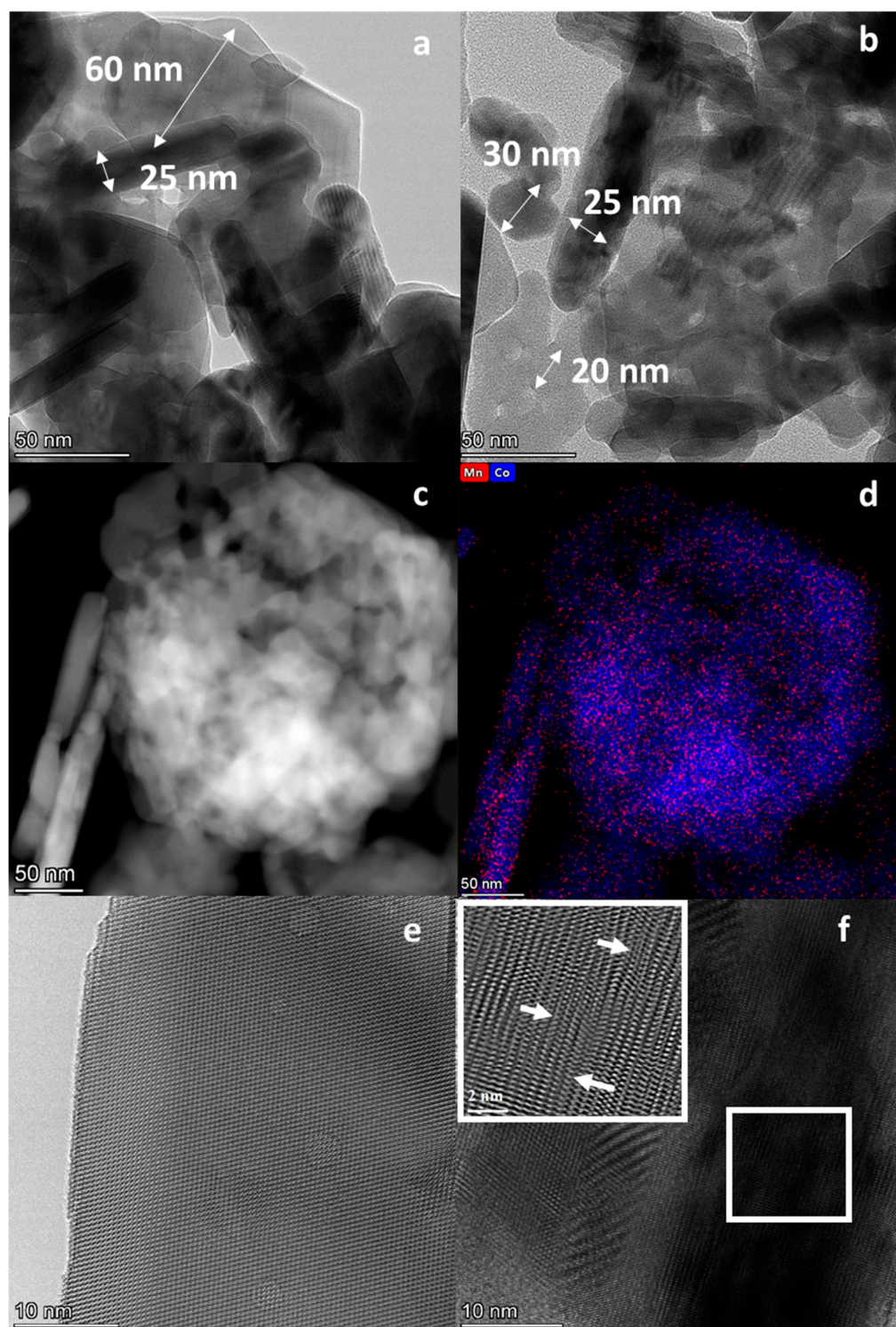


**Figure 3.** TEM images for  $\text{Co}_3\text{O}_4$  (a,e) and  $\text{Mn}_{0.1}\text{Co}_{2.9}$  (b–d,f). EDS mapping pattern of Mn (red) and Co (blue). Arrows indicate the strains.

### 2.3. EXAFS

EXAFS measurements were conducted to study the detailed structure of the catalysts. EXAFS analysis of  $\text{Co}_3\text{O}_4$  is complicated due to the presence of two nonequivalent octahedral and tetrahedral Co sites in the crystal structure. The  $\text{Co}_3\text{O}_4$  spinel consists of  $\text{Co}^{\text{Oh}}$  ions (Oh, octahedral coordination by six oxygen atoms) and  $\text{Co}^{\text{Td}}$  ions (Td, tetrahedral coordination by four oxygen atoms). These two oxygen shells of neighbors must be taken into account separately in order to make a reliable analysis of the data. Therefore,

a multisite-multishell analysis was performed due to the presence of non-equivalent Co sites. However, EXAFS averages over all the Co atoms in  $\text{Co}_3\text{O}_4$ , and only two-thirds of the Co atoms occupy octahedral sites; the remaining one-third occupies the tetrahedral ones. During refining, the coordination numbers (CN) in the EXAFS analysis of  $\text{Co}_3\text{O}_4$  were 4 instead of 6 for the octahedral  $\text{Co}^{\text{Oh}}$  site and 1.33 instead of 4 for the tetrahedral  $\text{Co}^{\text{Td}}$  site.

Two distributions for the first oxygen coordination shell,  $\text{Co}^{\text{Td}}\text{-O}$  and  $\text{Co}^{\text{Oh}}\text{-O}$ , and two distributions for the second cobalt coordination shell,  $\text{Co}^{\text{Oh}}\text{-Co}(\text{Mn})^{\text{Oh}}$  and  $\text{Co}^{\text{Oh}}\text{-Co}^{\text{Td}}$ , were then considered. The coordination shell  $\text{Co}^{\text{Td}}\text{-Co}^{\text{Td}}$  was not included in the analysis because it is rather larger than the cutoff distance included in the theoretical model.

The Fourier transform (FT) of the  $k^2$ -weighted EXAFS spectra of the  $\text{Mn}_x\text{Co}_{3-x}$  oxides with  $x = 0.1, 0.3, 0.7$ , and  $1.1$  is shown in Figure 4. The EXAFS data showed a peak at about  $1.45 \text{ \AA}$ , corresponding to the first oxygen coordination shell, and two further peaks between  $2.4$  and  $3.0 \text{ \AA}$ , mainly related to the nearest  $\text{M}^{\text{Oh}}\text{-M}^{\text{Oh}}$  (of  $2.9 \text{ \AA}$  in radius) and  $\text{M}^{\text{Td}}\text{-M}^{\text{Oh}}$  (of  $3.4 \text{ \AA}$  in radius) neighbors, respectively ( $\text{M} = \text{Mn}$  or  $\text{Co}$ ). For Co K-edge, the intensity of peaks in the area of  $2.5\text{--}3 \text{ \AA}$  decreased noticeably as  $x$  increased, which indicates a decrease in the amount of cobalt in the catalysts. Whereas for the Mn K-edge, the peak at  $3 \text{ \AA}$  was less intense than one at  $2.4 \text{ \AA}$ . This result indicates that Mn atoms mainly occupy the octahedral  $\text{Mn}^{\text{Oh}}$  site; so, for the Mn K-edge, the theoretical model only included scattering from the  $\text{Mn}^{\text{Oh}}$  site.

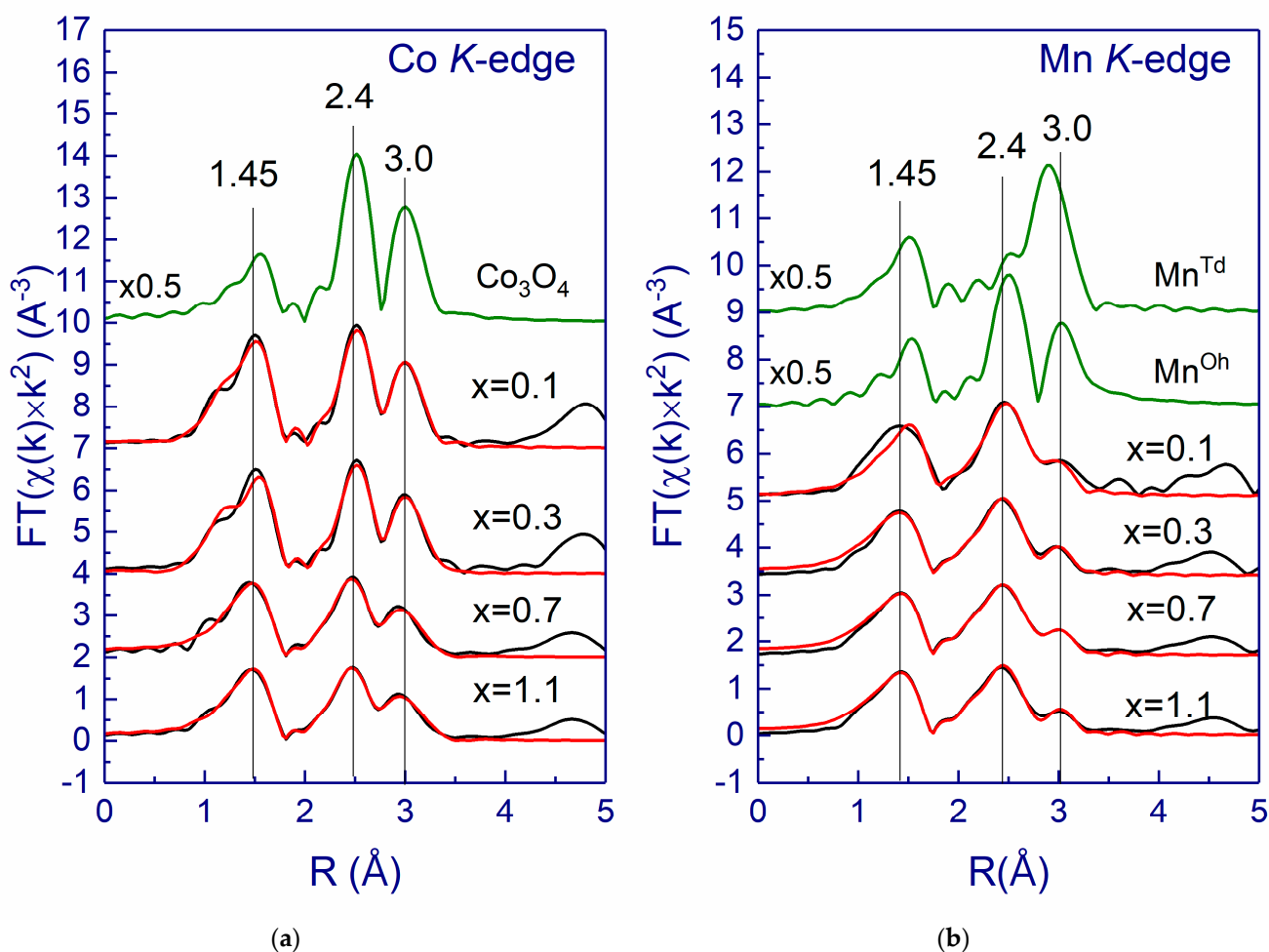


**Figure 4.** The Co (a) and Mn (b) K-edges EXAFS data (black line) and theoretical fits (red line) of the  $\text{Mn}_x\text{Co}_{3-x}$  ( $x = 0.1, 0.3, 0.7, 1.1$ ) oxides. The green line represents the theoretical magnitude curve of the Fourier transform (FT) of EXAFS for multisite-multishell Co sites in  $\text{Co}_3\text{O}_4$  (Co K-edge) and separately for  $\text{Mn}^{\text{Td}}$  and  $\text{Mn}^{\text{Oh}}$  sites (Mn K-edge).

The results of the quantitative analysis of the  $Mn_xCo_{3-x}$  catalysts are listed in Table 2, and the corresponding curve-fitting results of Co K-edge and Mn K-edge EXAFS are shown in Figure 4. These results confirmed that the best fit corresponded to the model without  $Mn^{Td}$  atoms. Since two Co-O distances (tetrahedral (1.89 Å) and octahedral (1.94 Å) sites) cannot be distinguished, these two Co-O pairs were fitted with a single path at an intermediate distance of 2.95 Å and total CN of 5.3, which was implemented for  $x = 0.1$ . The fits demonstrated that the total CN for  $Co^{Td}$  and  $Co^{Oh}$  decreased with increasing  $x$ , which was consistent with a decrease in the concentration of Co atoms in the samples.

**Table 2.** The EXAFS fit results: coordination numbers (CN), interatomic distances  $R$  (Å), and Debye–Waller factors  $\sigma^2$  (Å<sup>2</sup>), studied with EXAFS, compared to the crystal structure data of  $Co_3O_4$  (ICSD No. 290720), R-factor.

Catalyst	x = 1.1		x = 0.7		x = 0.3		x = 0.1		Co <sub>3</sub> O <sub>4</sub>	
	CN	R, Å	CN	R, Å	CN	R, Å	CN	R, Å	CN	R, Å
Co <sup>Td</sup> -O									1.3	1.893
Co <sup>Oh</sup> -O	4.2	1.932	4.8	1.931	4.6	1.928	5.0	1.903	4.0	1.942
Co <sup>Oh</sup> -Co/Mn <sup>Oh</sup>	4.3	2.883	5.5	2.885	6.5	2.880	7.5	2.873	4.0	2.858
Co <sup>Oh</sup> -Co <sup>Td</sup>	4.2	3.420	5.0	3.408	5.0	3.391	8.7	3.347	8.0	3.352
Co <sup>Td</sup> -O	3.1	3.296	3.1	3.280	2.8	3.267	5.8	3.264	5.3	3.374
Co <sup>Oh</sup> -Mn	1.5	3.050	2.3	3.074	3.4	3.070	6.3	3.107	–	–
<b>Mn K-edge Shell</b>	<b>CN</b>	<b>R, Å</b>	<b>CN</b>	<b>R, Å</b>	<b>CN</b>	<b>R, Å</b>	<b>CN</b>	<b>R, Å</b>	<b>CN</b>	<b>R, Å</b>
Mn <sup>Oh</sup> -O	2.7	1.908	2.8	1.913	1.8	1.870	1.8	1.912	6	1.942
Mn <sup>Oh</sup> -O	0.8	2.009	0.8	2.001	1.9	1.980	1.5	2.007	–	–
Mn <sup>Oh</sup> -Mn/Co <sup>Oh</sup>	3.8	2.924	4.4	2.922	3.8	2.903	4.8	2.884	6	2.858
Mn <sup>Oh</sup> -Co <sup>Td</sup>	3.4	3.420	3.2	3.408	2.9	3.391	4.6	3.385	6	3.352
Mn <sup>Oh</sup> -O	4.6	3.581	3.8	3.583	3.2	3.556	4.5	3.533	6	3.551
$\sigma^2$ (M-O), Å <sup>2</sup>	0.00386		0.00464		0.00240		0.00250			
$\sigma^2$ (M-M), Å <sup>2</sup>	0.00566		0.00646		0.00476		0.00577			
R-factor, %	1.16		1.25		1.88		3.43		–	

The first coordination shell,  $Mn^{Oh}$ , has an octahedral environment with four oxygen atoms at a distance of  $\sim 1.9$  Å. We were able to distinguish two  $Mn^{Oh}$ -O distances. Consequently, two distinct oxygen shells  $Mn^{Oh}$ -O samples were studied.

In regards to the structural parameters of the second coordination shell around  $Co^{Oh}$  and  $Mn^{Oh}$  obtained by EXAFS, the interatomic distance  $Co^{Oh}$ - $Co/Mn^{Oh}$  between edge-sharing  $Co^{Oh}$  octahedra (double-corner sharing between  $Co^{Oh}$  octahedra) remained almost constant and equal to 2.87–2.88 Å. The CN decreased from 7.5 to 4.3, while a similar distance  $Mn^{Oh}$ - $Mn/Co^{Oh}$  increased significantly from 2.88 to 2.92 Å, and CN remained virtually unchanged. The edge-sharing  $Mn^{Oh}$  octahedra tend to distance themselves from each other. The interatomic  $Co^{Oh}$ - $Co^{Td}$  distance (single-corner sharing between a tetrahedron and its nearest octahedron neighbor) increased from 3.35 to 3.42 Å as the  $x$  increased. The CN for  $Co^{Oh}$ - $Co^{Td}$  displayed a decrease, whereas the CN for  $Mn^{Oh}$ - $Co^{Td}$  increased, suggesting disordered Co vacancies, which is correlated to the decrease in the Co atoms.

FT of the Co data shows two apparent Co–Co contributions that could be fitted using two shells at approximately 2.86 and 3.35 Å. However, the best fits were obtained using a three-shell fit solution that yields Co–Co distances at around 2.9, 3.1, and 3.4 Å for all the



samples. The EXAFS fitting results indicated that there was an additional scattering path  $\text{Co}^{\text{Oh}}\text{-Mn}$  of around 3.05–3.10 Å in the radius, and it was added to the structural model, leading to additional local disorder in the structure.

The EXAFS results for the  $\text{Mn}_x\text{Co}_{3-x}$  catalysts confirm the formation of solid solutions and show that the addition of manganese ions to cobalt oxide provokes local distortions, and Mn ions prefer to occupy octahedral sites in the spinel structure.

#### 2.4. Catalyst Reducibility

Figure 5 shows TPR curves for the  $\text{Mn}_x\text{Co}_{3-x}$  catalysts. The TPR profile of pure  $\text{Co}_3\text{O}_4$  ( $x = 0$ ) exhibited two peaks of hydrogen consumption with maxima at 320 and 370 °C. Two peaks of hydrogen consumption corresponded to the two-step reduction:  $\text{Co}_3\text{O}_4 + \text{H}_2 \rightarrow 3\text{CoO} + \text{H}_2\text{O}$  and  $\text{CoO} + \text{H}_2 \rightarrow \text{Co} + \text{H}_2\text{O}$  [19,20]. With an increase in  $x$  and the incorporation of manganese cations into the cobalt oxide structure, these peaks shifted to a high-temperature region and became broader. A detailed description of the reduction process for mixed  $\text{Mn}_x\text{Co}_{3-x}\text{O}_4$  oxides can be found in the works in [21,22], illustrating that the addition of manganese to cobalt oxide inhibits the catalyst reduction. The reduction of  $\text{Mn}_x\text{Co}_{3-x}\text{O}_4$  mixed oxides proceeds via two stages: (1)  $\text{Mn}_x\text{Co}_{3-x}\text{O}_4 + \text{H}_2 \rightarrow 3(\text{Mn}_x\text{Co}_{3-x})_{1/3}\text{O} + \text{H}_2\text{O}$  and (2)  $3(\text{Mn}_x\text{Co}_{3-x})_{1/3}\text{O} + 3\text{H}_2 \rightarrow x\text{MnO} + (3-x)\text{Co} + 3\text{H}_2\text{O}$  [21,22].

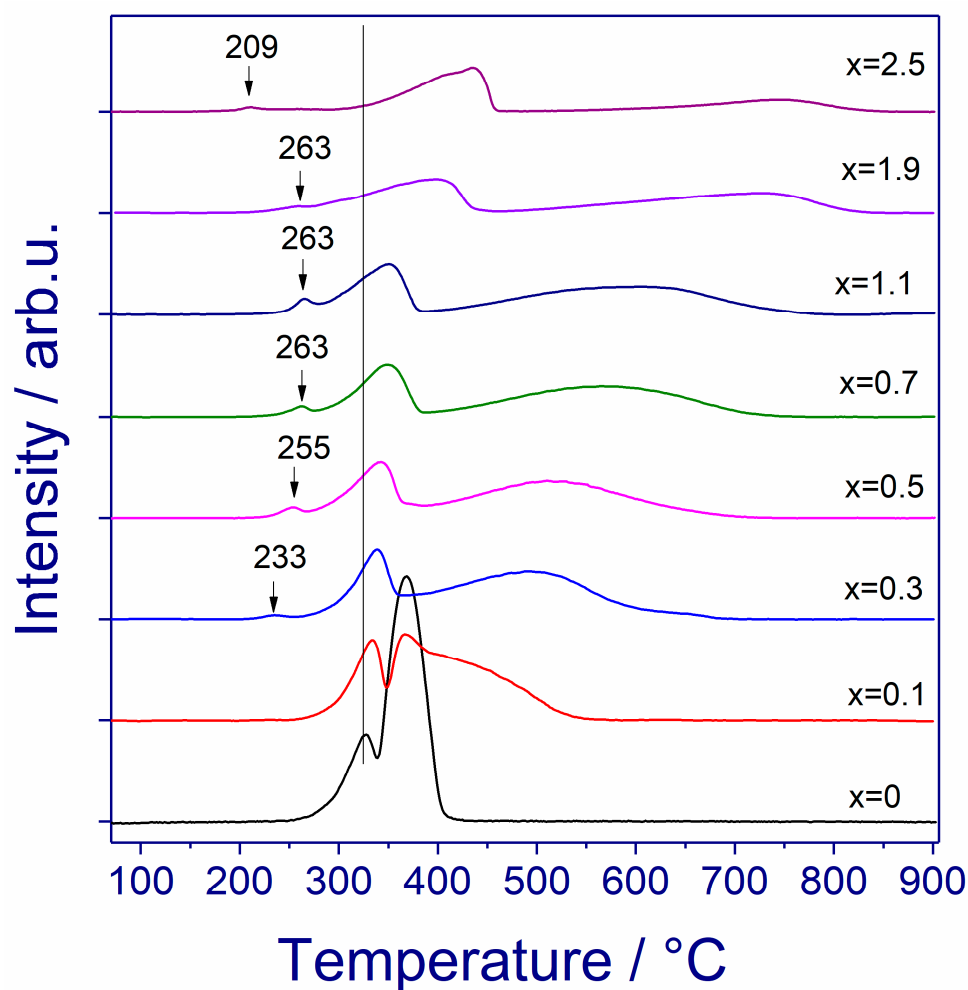


**Figure 5.** TPR- $\text{H}_2$  profiles of the  $\text{Mn}_x\text{Co}_{3-x}$  catalysts ( $x = 0, 0.1, 0.3, 0.4, 0.7, 1.1, 1.9, 2.5$ ). The black line shows the position of the first TPR peak of  $\text{Co}_3\text{O}_4$ .

With an increase in the Mn content from  $x = 0$  to  $x = 2.5$ , the total amount of consumed hydrogen decreased from 17.3 to 6.6 mmol  $H_2/g$  due to the reduction of cobalt oxide to  $Co^0$  and manganese oxide to  $Mn^{2+}$ . In the case of  $x = 0.3$ – $2.5$ , the appearance of small low-temperature peaks at 209–263 °C was observed. Low-temperature peaks were associated with the reduction of amorphized or highly dispersed oxides, which were undetectable by XRD [23,24]. Previously, it was shown that the TPR curve for  $Mn_5Co_1O_x$  catalysts prepared at 400 °C contains an intense hydrogen consumption peak at 270 °C, which is associated with the reduction of  $MnCoO_3$  [14]. Zhang et al. found that for the  $Co_2Mn_1O_x$  catalyst calcined at the temperature range of 300–700 °C, weak low-temperature TPR peaks at 180–240 °C were observed [6]. The reduction bands were assigned to the reduction of easily reducible species (highly dispersed surface  $Mn^{4+}$  species produced by nano Co-Mn oxide composites and adsorbed oxygen species). The authors correlate the low-temperature reducibility to the catalytic activity in the oxidation of CO and benzene [6,14]. In our case, the proportion of the low-temperature peak to the total hydrogen consumption was 0.3–4%. Low-temperature peaks of hydrogen consumption were not observed for the most active  $Mn_{0.1}Co_{2.9}$  catalyst. It is worth noting that the presence of low-temperature peaks on TPR profiles did not correlate with the catalytic activity.

## 2.5. XPS

To study the chemical states and relative concentrations of elements in the (sub)surface layers of the  $Mn_xCo_{3-x}$  catalysts, XPS was applied. Figure 6a shows the Mn 2*p* core-level spectra of the studied catalyst at different concentrations of Mn. To identify the manganese state, we used the binding energy of the  $Mn2p_{3/2}$  peak, the presence and position of shake-up satellites [25–27], and the magnitude of the multiplet splitting of the Mn3*s* level. Figure S1 shows Mn3*s* and O1*s* core-level spectra of the studied catalysts. The fitting of Mn2*p* spectra allowed us to reveal that manganese was present in the  $Mn^{2+}$ ,  $Mn^{3+}$ , and  $Mn^{4+}$  states and by the satellites located, respectively, at a distance of 6.6, 10.5, and 11.8 eV from the main peaks. The binding energies of  $Mn2p_{3/2}$  peaks equal to 640.2, 641.5, and 642.6 eV were assigned to the  $Mn^{2+}$ ,  $Mn^{3+}$ , and  $Mn^{4+}$  states, respectively. According to the literature, manganese in MnO,  $Mn_2O_3$ , and  $MnO_2$  oxides is characterized by the  $Mn2p_{3/2}$  binding energy for MnO,  $Mn_2O_3$ , and  $MnO_2$  oxides in the ranges of 640.4–641.7, 641.5–641.9, and 642.2–642.6 eV, respectively, and the Mn3*s* multiplet splitting: MnO (5.6–5.8 eV),  $Mn_2O_3$  (5.2–5.4 eV),  $MnO_2$  (4.5–4.7 eV) and  $Mn_3O_4$  (5.3–5.6 eV) [25,27–29].

Figure 6b shows the Co2*p* spectra of the  $Mn_xCo_{3-x}$  catalysts. The spectra consist of the  $Co2p_{3/2}$ – $Co2p_{1/2}$  doublet and the corresponding shake-up satellites. To identify the chemical state of cobalt, the position of the  $Co2p_{3/2}$  main line and the shape of the Co2*p* spectrum (the intensity and the relative position of the shake-up satellites) should be used. In the literature, the  $Co2p_{3/2}$  binding energies reported for metallic cobalt, CoO, and  $Co_3O_4$  oxides are in the range of 778.0–778.1 eV, 780.0–780.5 eV, and 779.6–780.7 eV, respectively [30,31]. The wide range of binding energies observed in the  $Co2p_{3/2}$  spectra of  $Co_3O_4$  was attributed to the presence of  $Co^{2+}$  and  $Co^{3+}$ . The literature values for the binding energies of these cations are 780.0–780.9 eV for  $Co^{2+}$  and 779.4–779.6 eV for  $Co^{3+}$  [32,33]. The Co2*p* spectra of CoO and  $Co_3O_4$  oxides differ in satellite peaks, which allows us to distinguish these two oxides. This discrepancy is due to varying coordination environments for cobalt cations in CoO and  $Co_3O_4$  [32]. In the case of CoO, two intense satellite peaks were observed at the energy separations that were 2 eV and 6 eV higher than the main  $Co2p_{3/2}$  peak.

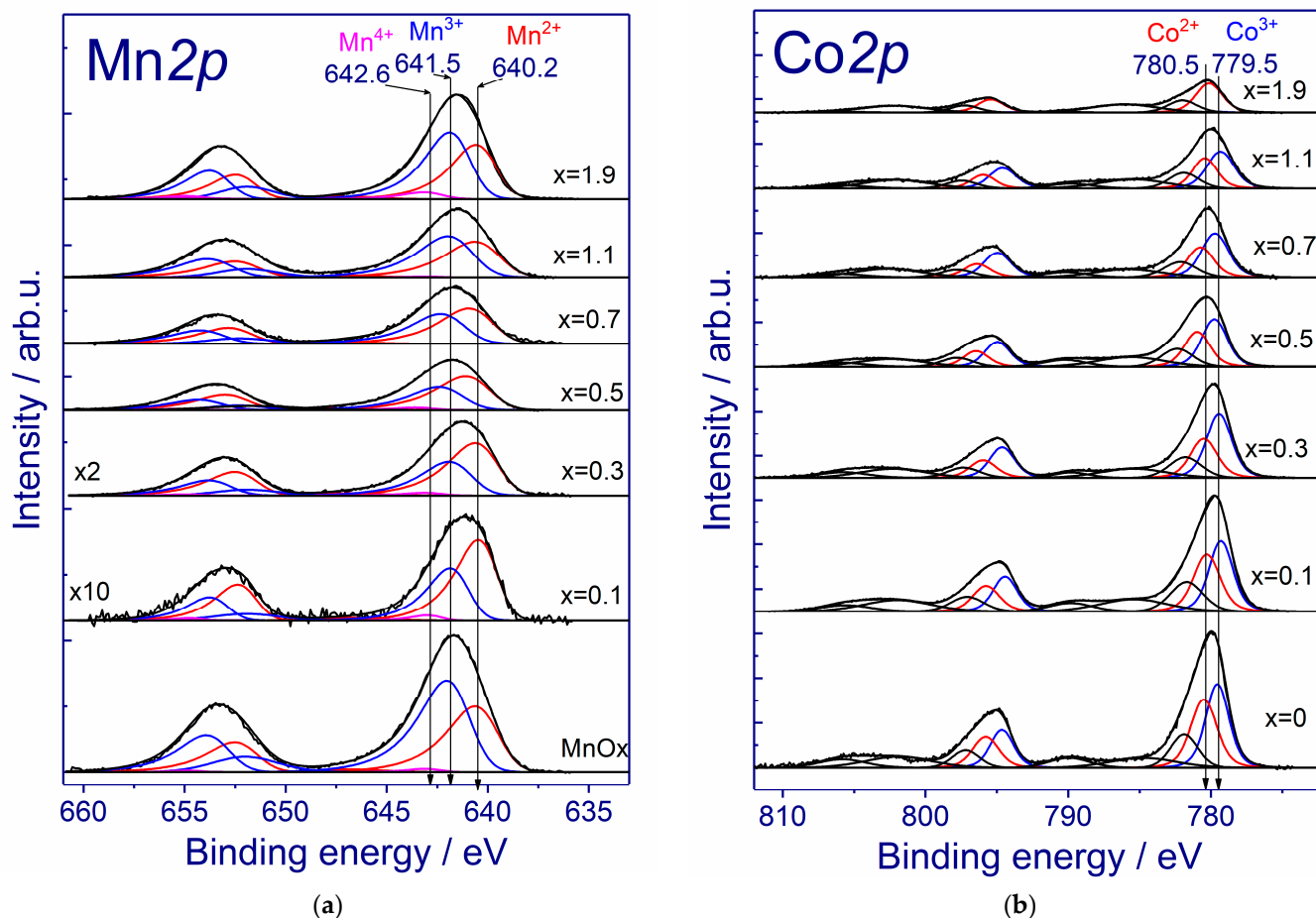


**Figure 6.** Mn2p (a) and Co2p (b) core-level spectra of the studied catalysts. The spectra are normalized to the total integrated intensity of the corresponding Mn2p and Co2p spectra.

In contrast, the Co2p spectrum of Co<sub>3</sub>O<sub>4</sub> exhibited three satellite peaks located at 2 eV, 6 eV, and 10 eV above the Co2p<sub>3/2</sub> peak. Furthermore, the second satellite peak in the spectrum of Co<sub>3</sub>O<sub>4</sub> had a much lower intensity compared to CoO. The shape of the Co2p core-level spectrum and the position of the Co2p<sub>3/2</sub> peak at 780.2 eV in the Mn<sub>1.9</sub>Co<sub>0.1</sub> catalyst indicate that cobalt was present in the Co<sup>2+</sup> oxidation state. In contrast, in all other catalysts, cobalt existed in both the Co<sup>2+</sup> and Co<sup>3+</sup> oxidation states. The binding energies of the Co2p<sub>3/2</sub> peaks corresponding to Co<sup>2+</sup> and Co<sup>3+</sup> cations in the obtained spectra were approximately 780.5 and 779.5 eV, respectively. Analysis of the Co2p core-level spectra of the studied samples indicated that in the Mn<sub>1.9</sub>Co<sub>0.1</sub> catalyst, cobalt was present in the Co<sup>2+</sup> oxidation state, whereas, in all other catalysts, cobalt could exist in both the Co<sup>2+</sup> and Co<sup>3+</sup> oxidation states. The XPS analysis allowed us to estimate the fraction of manganese and cobalt in different oxidation states (Table 3). It was obvious that with increasing *x*, the surface concentration of [Mn]/[Co + Mn] increased. For all compositions, the surface was enriched with manganese cations compared to the stoichiometric one. For example, the Mn<sub>0.1</sub>Co<sub>2.9</sub> catalyst contained the stoichiometric ratio of [Mn]/[Co + Mn] = 0.03, and the experimental value was 0.07. The introduction of Mn ions into cobalt oxide led to a redistribution of the surface concentration of Co<sup>2+</sup> and Co<sup>3+</sup> cations. The surface ratio [Co<sup>3+</sup>]/[Co<sup>3+</sup>] was maximum for the Mn<sub>0.1</sub>Co<sub>2.9</sub> sample. With an increase in *x* from 0 to 0.1–0.3, the Co<sup>3+</sup> content increased from 52 to 63%; a further increase in *x* to 0.5–1.1 resulted in a decrease in Co<sup>3+</sup> to 30–50%. For *x* = 1.9 and *x* = 2.5, only Co<sup>2+</sup> was observed in the catalyst composition, which was in good agreement with the literature data, indicating that

with a small amount of Co, it predominantly replaced  $\text{Mn}^{2+}$  in tetrahedral positions and was in the oxidation state of 2+ [34,35].

**Table 3.** Atomic ratios of elements on the catalyst surface and the binding energy values for  $\text{Mn}2p_{3/2}$ ,  $\text{Co}2p_{3/2}$ , and  $\Delta\text{Mn}3s$ .

Catalyst	$\text{Mn}2p_{3/2}$			$\text{Co}2p_{3/2}$		[Mn]/ [Co + Mn]	$\Delta\text{Mn}3s$ , eV
	$\text{Mn}^{2+}$ , eV (%)	$\text{Mn}^{3+}$ , eV (%)	$\text{Mn}^{4+}$ , eV (%)	$\text{Co}^{2+}$ , eV (%)	$\text{Co}^{3+}$ , eV (%)		
$\text{Co}_3\text{O}_4$	-	-	-	780.5 (45%)	779.6 (56%)	0.00	-
$\text{Mn}_{0.1}\text{Co}_{2.9}$	640.1 (57%)	641.6 (40%)	642.6 (3%)	780.5 (37%)	779.5 (63%)	0.07	-
$\text{Mn}_{0.3}\text{Co}_{2.7}$	640.2 (57%)	641.5 (40%)	642.6 (3%)	780.5 (39%)	779.5 (61%)	0.26	5.7
$\text{Mn}_{0.5}\text{Co}_{2.5}$	640.2 (55%)	641.5 (41%)	642.6 (3%)	780.5 (41%)	779.5 (59%)	0.37	5.4
$\text{Mn}_{0.7}\text{Co}_{2.3}$	640.2 (51%)	641.5 (48%)	642.6 (1%)	780.5 (38%)	779.6 (62%)	0.40	5.5
$\text{Mn}_{1.1}\text{Co}_{1.9}$	640.2 (44%)	641.5 (56%)	642.6 (1%)	780.4 (41%)	779.5 (59%)	0.46	5.6
$\text{Mn}_{1.9}\text{Co}_{1.1}$	640.2 (41%)	641.5 (54%)	642.6 (5%)	780.2 (100%)	779.5 (0%)	0.70	5.5
$\text{Mn}_{2.5}\text{Co}_{0.5}$	640.1 (15%)	641.4 (65%)	642.6 (20%)	780.5 (100%)	-	0.83	5.4
$\text{MnO}_x$	640.2 (40%)	641.6 (59%)	642.6 (1%)	-	-	1.00	5.5

### 3. Discussion

Overall, the strong synergetic effect between Mn and Co species in a solid solution plays a key role in catalytic activity [7,10,12,13]. Cooperation between two elements changes the chemical, structural, and microstructural properties of the catalyst. Generally, parameters such as specific surface area, crystallite size, pore system, good low-temperature redox property, and active oxygen species are relevant to the good activity of Mn-Co oxide catalysts for oxidation reactions [6,8–13,22]. The methods of preparation and the ratio between elements can adjust these parameters. Since the interactions between different components are usually complicated, the introduction of an additional element changes several characteristics of the catalyst at once, so it is not possible to vary only one characteristic and fix other ones. Such behavior complicates the interpretation of the results and makes it difficult to determine the role of each factor. In the case of Co-Mn oxide catalysts, solid solutions are formed based on the spinel structure; however, the formation of highly dispersed or amorphous oxides is also possible [14]. In this work, we investigated the catalytic properties of mixed Mn-Co oxides with a spinel structure. In order to avoid the presence of amorphous highly dispersed states, we used a relatively high temperature of 600 °C. As a result, for  $x = 0 \dots 1.1$ , a  $\text{Mn}_x\text{Co}_{3-x}\text{O}_4$  oxide was formed with a cubic spinel structure, while for  $x = 1.9$  and 2.5, a  $\text{Mn}_x\text{Co}_{3-x}\text{O}_4$  with a tetragonal spinel structure was observed. For only the  $\text{Mn}_{1.9}\text{Co}_{1.1}$  catalyst, the appearance of a 4 wt %  $\text{CoMnO}_3$  was observed (Table 1). The TPR curves illustrate the reduction of  $\text{Mn}_x\text{Co}_{3-x}\text{O}_4$  oxide (Figure 5), whereas the low-temperature peaks of hydrogen consumption were detected, but the intensity of these peaks was less than 4%. This means the preferential formation of a mixed oxide

with a spinel structure. For  $x = 1.1$ – $1.9$ , the catalysts contained two phases, both cubic and tetragonal spinel [21].

An analysis of the catalytic activity in CO oxidation showed that the activity decreases in the following series:  $\text{Mn}_{0.1}\text{Co}_{2.9} > \text{Co}_3\text{O}_4 \sim \text{Mn}_{0.3}\text{Co}_{2.7} > \text{Mn}_{0.5}\text{Co}_{2.5} > \text{MnO}_x > \text{Mn}_{0.7}\text{Co}_{2.3} > \text{Mn}_{0.9}\text{Co}_{2.1} \sim \text{Mn}_{1.1}\text{Co}_{1.9} \sim \text{Mn}_{2.5}\text{Co}_{0.5} > \text{Mn}_{2.9}\text{Co}_{0.1} > \text{Mn}_{1.7}\text{Co}_{1.3} > \text{Mn}_{2.1}\text{Co}_{0.9} > \text{Mn}_{1.3}\text{Co}_{1.7} \sim \text{Mn}_{1.5}\text{Co}_{1.5} \sim \text{Mn}_{2.3}\text{Co}_{0.7}$ . The addition of manganese cations into cobalt oxide led to a decrease in  $T_{50}$  from 129 to 97 °C (Figure 1). For  $x = 0.3$ – $0.7$ , the activity of  $\text{Mn}_x\text{Co}_{3-x}$  catalysts was located between the corresponding values for pure oxides. Interestingly, for  $x > 1.1$ , the activity was less than for pure oxide  $\text{MnO}_x$ . The nature of this effect is likely due to two factors leading to an increase or decrease in catalytic activity: (i) the dilution of the catalyst with manganese reduces its catalytic activity since  $\text{Co}_3\text{O}_4$  is more active than  $\text{MnO}_x$  (Figure 1), and (ii) the addition of manganese ions alters the microstructure and structure properties of cobalt oxide, leading to an improvement of catalytic performance. The addition of Mn ions into cobalt oxide resulted in a decrease in the crystal size from 550 Å ( $x = 0$ ) to 160 Å ( $x = 1.1$ ) and growth of the strains from 0.14% ( $x = 0$ ) to 0.36% ( $x = 1.1$ ) and surface area from 25 m<sup>2</sup>/g ( $x = 0$ ) to 44 m<sup>2</sup>/g ( $x = 1.1$ ) (Table 1). The EXAFS results showed that Mn ions replaced Co ions in the octahedral position in the spinel structure, leading to a local distortion. Our observations are in good agreement with the literature data. Mitran et al. [36] found that the substitution of Co with Mn in the cubic phase of a spinel structure leads to the appearance of network defects as oxygen vacancies, observed from the evaluation of lattice deformation where the elastic strain increases with Mn content. The  $\text{Co}^{3+}$  cations are substituted by  $\text{Mn}^{3+}$  and  $\text{Mn}^{4+}$  cations in octahedral sites [36]. The most active catalyst,  $\text{Mn}_{0.1}\text{Co}_{2.9}$ , is characterized by a small crystal size of mixed oxide (220 Å) and the maximum amount of the surface concentration of  $\text{Co}^{3+}$  ions (Table 3). Several works showed that the catalytic activity of cobalt oxides was due to  $\text{Co}^{3+}$  ions in octahedral sites [37,38]. Probably, in the case of the most active catalyst, the effect of changes in structure and microstructure characteristics is more significant than changes in the surface chemical composition ( $\text{Co}^{3+}$  ions in octahedral sites).

On the other hand, the introduction of cobalt into manganese oxide did not improve the catalytic performance (Figure 1). It is worth noting here that the  $\text{MnO}_x$  sample contained several phases; in addition to spinel  $\text{Mn}_3\text{O}_4$ , there were 10 wt %  $\text{Mn}_2\text{O}_3$  and 35 wt %  $\text{Mn}_5\text{O}_8$  oxides. From this point of view, it is not entirely correct to analyze the incorporation of cobalt into  $\text{Mn}_3\text{O}_4$  oxide and compare it with  $\text{MnO}_x$  catalysts. Hence, for low cobalt content, it is expected that the catalytic activity does not change much because the substitution occurs only in the inactive tetrahedral sites where  $\text{Co}^{2+}$  replaces  $\text{Mn}^{2+}$ . When the tetrahedral sites are fully occupied by  $\text{Co}^{2+}$  ( $x > 1$ ), the substitution occurs in the octahedral sites, creating active  $\text{Co}^{3+}$  ions [35].

## 4. Materials and Methods

### 4.1. Catalyst Preparation

The catalysts with different Mn content were prepared using the coprecipitation method. The calculated amount of  $\text{Co}(\text{NO}_3)_2$  and  $\text{Mn}(\text{NO}_3)_2$  aqueous solutions was poured into a round-bottom flask. The precipitation was carried out under stirring with a gradual addition of a NaOH solution to bring the pH of the solution to 11. After subsequent aging, the precipitate was filtered, washed with distilled water on a filter to pH 6, dried at 120 °C, and calcined in air at 600 °C for 4 h. The catalysts were designated as  $\text{Mn}_x\text{Co}_{3-x}$ , where  $x$  is the molar fraction of manganese.

#### 4.2. Catalyst Characterization

The phase composition was determined by XRD using a STOE STADI MP diffractometer equipped with a Mythen2 1K (Dectris, Baden, Switzerland) linear detector. The diffraction patterns were obtained in transmission  $\theta/2\theta$  geometry in the  $2\theta$  range from 4 to 32° with a step of 0.015° using monochromatic MoK $_{\alpha 1}$  radiation ( $\lambda = 0.7093 \text{ \AA}$ , Ge crystal monochromator). The Rietveld refinement for quantitative analysis was carried out using the software package Topas V.4.2. TOPAS supports the Double-Voigt Approach where crystallite size and strain comprise Lorentzian and Gaussian component convolutions varying in  $2\theta$  as a function of  $1/\cos(\theta)$  and  $\tan(\theta)$  respectively. The instrumental broadening was described with LaB $_6$  as a reference material. The crystallite size was calculated using LVol-IB values (LVol-IB—the volume-weighted mean column height based on integral breadth). The phases were identified using the powder diffraction database PDF-4+.

The specific surface area was calculated using the Brunauer–Emmett–Teller (BET) method using nitrogen adsorption isotherms measured at liquid nitrogen temperatures with an automatic Micromeritics ASAP 2400 sorptometer (Norcross, GA, USA).

TEM images were obtained using a ThemisZ Thermo Fisher Scientific microscope (Thermo Fisher Scientific, Eindhoven, The Netherlands) with a resolution of 0.7 Å, respectively. Elemental maps were obtained using the energy-dispersive spectrometer SuperX, Thermo Fisher Scientific. Samples for research were fixed on standard copper grids using ultra-sonic dispersion of the catalysts in ethanol.

Co and Mn K-edge X-ray absorption spectra were measured at the Synchrotron Radiation Source. The radiation was monochromatized using a water-cooled double-crystal monochromator with Si(111) single-crystal pairs. The powdered sample was pressed between two Kapton<sup>®</sup> films (DuPont, PA, USA). Co and Mn K-edge XANES spectra were recorded in the transmission mode using ionization chambers, and the absorption spectra of Co or Mn foils were measured simultaneously with the sample spectrum using a third ionization chamber, as commonly applied in XAS experiments for energy calibration. The extended X-ray absorption fine structure (EXAFS) data were preprocessed and normalized according to standard procedures in the Demeter [39] program of the IFEFFIT 2.0 software package [40]. The EXAFS spectra were quantitatively analyzed, and a nonlinear best fit was performed for the Fourier-transformed  $k^2$ -weighted experimental XAFS signals. The fitting procedure employs both the imaginary and real parts of the Fourier-transformed EXAFS oscillations and minimizes the difference between the normalized experimental data and the theoretical EXAFS obtained by ab initio multiple-scattering calculation for the given crystal structure model using the FEFF6 code.

The temperature-programmed reduction in hydrogen (TPR-H $_2$ ) was performed with 40–60 mg of sample in a quartz reactor using a flow setup with a thermal conductivity detector. The reducing mixture (10 vol.% of H $_2$  in Ar) was fed at a rate of 40 mL/min. The rate of heating from room temperature was 10°/min.

XPS analysis was performed on an X-ray photoelectron spectrometer (SPECS Surface Nano Analysis GmbH, Berlin, Germany) equipped with an XR-50M X-ray source having a twin Al/Ag anode, a FOCUS-500 X-ray monochromator (SPECS Surface Nano Analysis GmbH, Berlin, Germany), and a PHOIBOS-150 hemispherical electron energy analyzer (SPECS Surface Nano Analysis GmbH, Berlin, Germany). The core-level spectra were obtained using monochromatic MgK $\alpha$  radiation ( $h\nu = 1253.6 \text{ eV}$ ) under ultrahigh vacuum conditions. The charge correction was performed by setting the C1s peak at 284.8 eV. Relative concentrations of elements were determined from the integrated intensities of the core-level spectra using the cross sections according to Scofield [41]. For detailed analysis, the spectra were fitted into several peaks after the background subtraction by the Shirley

method [42]. The fitting procedure was performed using the CasaXPS software. The line shapes were approximated by the multiplication of Gaussian and Lorentzian functions.

#### 4.3. Catalytic Tests

Catalytic tests were performed in a flow regime using a glass reactor 170 mm in length and 10 mm in inner diameter. The initial gas mixture composition was 1 vol.% CO in air. The contact time was 0.12 s. All the samples were investigated in the temperature range of 50–350 °C. A catalyst fraction of 0.4–1.0 mm was used. To avoid overheating during the exothermic reaction, the catalyst was mixed with a quartz powder. The reactant mixture before and after the reactor was analyzed by a gas chromatograph equipped with a zeolite CaA column and a thermal conductivity detector.

## 5. Conclusions

A series of the  $Mn_xCo_{3-x}$  oxide catalysts were synthesized by coprecipitation method with further calcination at 600 °C with varying manganese content from  $x = 0$  to  $x = 3$ . For  $x = 0 \dots 1.1$ ,  $Mn_xCo_{3-x}O_4$  oxide was formed with a cubic spinel structure, while for  $x = 1.9$  and  $2.5$ ,  $Mn_xCo_{3-x}O_4$  with a tetragonal spinel structure was observed. Analysis of the catalytic activity in CO oxidation showed that the activity decreased in the following series:  $Mn_{0.1}Co_{2.9} > Co_3O_4 \sim Mn_{0.3}Co_{2.7} > Mn_{0.5}Co_{2.5} > MnO_x > Mn_{0.7}Co_{2.3} > Mn_{0.9}Co_{2.1} \sim Mn_{1.1}Co_{1.9} \sim Mn_{2.5}Co_{0.5} > Mn_{2.9}Co_{0.1} > Mn_{1.7}Co_{1.3} > Mn_{2.1}Co_{0.9} > Mn_{1.3}Co_{1.7} \sim Mn_{1.5}Co_{1.5} \sim Mn_{2.3}Co_{0.7}$ . The  $Mn_{0.1}Co_{2.9}$  catalyst displayed the best catalytic activity, which was attributed to its high surface area and maximum surface ratio between  $Co^{3+}$  and  $Co^{2+}$ . A further increase in the manganese content ( $x > 0.3$ ) provoked drastic changes in the catalytic properties due to a decrease in the cobalt content on the surface and in the volume of mixed oxide, changes in the oxidation states of cations, and structure transformation. It has been shown that the introduction of Mn into cobalt oxide has opposite effects on the catalytic properties; on the one hand, there is a change in microstructural properties (a decrease in the size of oxide particles and an increase in the specific surface area), the formation of micro strains, and distortions of the local environment. On the other hand, the introduction of manganese leads to a decrease in the cobalt content at the octahedral positions of spinel, which has a negative effect on the catalytic properties.

**Supplementary Materials:** The following supporting information can be downloaded at: <https://www.mdpi.com/article/10.3390/inorganics13010008/s1>, Figure S1.  $Mn3s$  and  $O1s$  core-level spectra of the studied catalysts. The spectra are normalized to the total integrated intensity of the corresponding  $Mn2p$  and  $Co2p$  spectra.

**Author Contributions:** Conceptualization, O.A.B.; formal analysis, E.Y.G., E.E.A., V.A.R., and A.M.K.; investigation, E.Y.G., O.A.B., E.E.A., V.A.R., and A.M.K. writing—original draft preparation, O.A.B. writing—review and editing, O.A.B.; visualization, O.A.B., A.M.K.; supervision, O.A.B. All authors have read and agreed to the published version of the manuscript.

**Funding:** This work was supported by the Ministry of Science and Higher Education of the Russian Federation (Grant Agreement No. 075-15-2022-263).

**Data Availability Statement:** The original contributions presented in this study are included in the article/Supplementary Material. Further inquiries can be directed to the corresponding author.

**Acknowledgments:** The experiments were performed using large-scale research facilities, “EXAFS spectroscopy beamline”, at the Siberian Synchrotron and Terahertz Radiation Center. The authors express their gratitude to T.N. Afanasenko for the synthesis of the catalyst.

**Conflicts of Interest:** Authors Olga A. Bulavchenko, Egor E. Aydakov and Anna M. Kremneva are employed by Synchrotron Radiation Facility SKIF. The authors of the paper declare that the research was conducted in the absence of any commercial or financial relationships that could be construed as a potential conflict of interest. The affiliated company was not involved in the study design, collection, analysis, interpretation of data, the writing of this article or the decision to submit it for publication.

## References

1. Royer, S.; Duprez, D. Catalytic Oxidation of Carbon Monoxide over Transition Metal Oxides. *ChemCatChem* **2011**, *3*, 24–65. [[CrossRef](#)]
2. Shen, Z.; Xing, X.; Wang, S.; Ren, S.; Lv, M.; Zheng, Z.; Jiang, X. Removal of CO in Flue Gas by Catalytic Oxidation: A Review. *Z. Für Phys. Chem.* **2024**, *238*, 1207–1265. [[CrossRef](#)]
3. Shi, J. On the Synergetic Catalytic Effect in Heterogeneous Nanocomposite Catalysts. *Chem. Rev.* **2013**, *113*, 2139–2181. [[CrossRef](#)]
4. Zhou, X.; Fang, S.; Zhang, T.; Wu, Z.; Li, J.; Wang, W.; Zhu, J.; Wu, J.; Ye, D.; Han, R.; et al. Unveiling the Mechanistic Synergy in Mn-Doped NiO Catalysts with Atomic-Burly Structure: Enhanced CO Oxidation via Ni-OH and Mn Bifunctionality. *Sep. Purif. Technol.* **2025**, *354*, 129330. [[CrossRef](#)]
5. Aukrust, E.; Muan, A. Phase Relations in the System Cobalt Oxide–Manganese Oxide in Air. *J. Am. Ceram. Soc.* **1963**, *46*, 511. [[CrossRef](#)]
6. Zhang, X.; Junhui, Y.; Jing, Y.; Ting, C.; Bei, X.; Zhe, L.; Kunfeng, Z.; Ling, Y.; Dannong, H. Excellent Low-Temperature Catalytic Performance of Nanosheet Co–Mn Oxides for Total Benzene Oxidation. *Appl. Catal. A Gen.* **2018**, *566*, 104–112. [[CrossRef](#)]
7. Tang, W.; Wu, X.; Li, S.; Li, W.; Chen, Y. Porous Mn–Co Mixed Oxide Nanorod as a Novel Catalyst with Enhanced Catalytic Activity for Removal of VOCs. *Catal. Commun.* **2014**, *56*, 134–138. [[CrossRef](#)]
8. Qu, Z.; Gao, K.; Fu, Q.; Qin, Y. Low-Temperature Catalytic Oxidation of Toluene over Nanocrystal-like Mn–Co Oxides Prepared by Two-Step Hydrothermal Method. *Catal. Commun.* **2014**, *52*, 31–35. [[CrossRef](#)]
9. Aguilera, D.A.; Perez, A.; Molina, R.; Moreno, S. Cu–Mn and Co–Mn Catalysts Synthesized from Hydrotalcites and Their Use in the Oxidation of VOCs. *Appl. Catal. B Environ.* **2011**, *104*, 144–150. [[CrossRef](#)]
10. Tang, W.; Li, W.; Li, D.; Liu, G.; Wu, X.; Chen, Y. Synergistic Effects in Porous Mn–Co Mixed Oxide Nanorods Enhance Catalytic Deep Oxidation of Benzene. *Catal. Lett.* **2014**, *144*, 1900–1910. [[CrossRef](#)]
11. Tannous, M.; Bounoukta, C.E.; Siffert, S.; Poupin, C.; Cousin, R. Total Catalytic Oxidation of Ethanol over MnCoAl Mixed Oxides Derived from Layered Double Hydroxides: Effect of the Metal Ratio and the Synthesis Atmosphere Conditions. *Catalysts* **2023**, *13*, 1316. [[CrossRef](#)]
12. Faure, B.; Alphonse, P. Co–Mn-Oxide Spinel Catalysts for CO and Propane Oxidation at Mild Temperature. *Appl. Catal. B Environ.* **2016**, *180*, 715–725. [[CrossRef](#)]
13. Liu, C.; Gong, L.; Dai, R.; Lu, M.; Sun, T.; Liu, Q.; Huang, X.; Huang, Z. Mesoporous Mn Promoted Co<sub>3</sub>O<sub>4</sub> Oxides as an Efficient and Stable Catalyst for Low Temperature Oxidation of CO. *Solid. State Sci.* **2017**, *71*, 69–74. [[CrossRef](#)]
14. Bulavchenko, O.A.; Afonassenko, T.N.; Sigaeva, S.S.; Ivanchikova, A.V.; Saraev, A.A.; Gerasimov, E.Y.; Kaichev, V.V.; Tsybulya, S.V. The Structure of Mixed Mn–Co Oxide Catalysts for CO Oxidation. *Top. Catal.* **2020**, *63*, 75–85. [[CrossRef](#)]
15. Frey, K.; Iablokov, V.; Sáfrán, G.; Osán, J.; Sajó, I.; Szukiewicz, R.; Chenakin, S.; Kruse, N. Nanostructured MnOx as Highly Active Catalyst for CO Oxidation. *J. Catal.* **2012**, *287*, 30–36. [[CrossRef](#)]
16. Iablokov, V.; Frey, K.; Geszti, O.; Kruse, N. High Catalytic Activity in CO Oxidation over MnO<sub>x</sub> Nanocrystals. *Catal. Lett.* **2010**, *134*, 210–216. [[CrossRef](#)]
17. Bulavchenko, O.A.; Afonassenko, T.N.; Osipov, A.R.; Pochtar, A.A.; Saraev, A.A.; Gerasimov, E.Y. The Formation of Mn–Ce Oxide Catalysts for CO Oxidation by Oxalate Route: The Role of Annealing Conditions. *Catal. Lett.* **2021**, *151*, 2906–2918. [[CrossRef](#)]
18. Shannon, R.D. Revised Effective Ionic Radii and Systematic Studies of Interatomic Distances in Halides and Chalcogenides. *Acta Cryst. A* **1976**, *32*, 751–767. [[CrossRef](#)]
19. Bulavchenko, O.A.; Cherepanova, S.V.; Malakhov, V.V.; Dovlitova, L.S.; Ishchenko, A.V.; Tsybulya, S.V. In Situ XRD Study of Nanocrystalline Cobalt Oxide Reduction. *Kinet. Catal.* **2009**, *50*, 192–198. [[CrossRef](#)]
20. Sexton, B. An XPS and TPR Study of the Reduction of Promoted Cobalt-Kieselguhr Fischer-Tropsch Catalysts. *J. Catal.* **1986**, *97*, 390–406. [[CrossRef](#)]
21. Bulavchenko, O.A.; Afonassenko, T.N.; Ivanchikova, A.V.; Murzin, V.Y.; Kremneva, A.M.; Saraev, A.A.; Kaichev, V.V.; Tsybulya, S.V. In Situ Study of Reduction of Mn<sub>x</sub> C<sub>3–x</sub> O<sub>4</sub> Mixed Oxides: The Role of Manganese Content. *Inorg. Chem.* **2021**, *60*, 16518–16528. [[CrossRef](#)] [[PubMed](#)]
22. Bulavchenko, O.A.; Gerasimov, E.Y.; Afonassenko, T.N. Reduction of Double Manganese–Cobalt Oxides: In Situ XRD and TPR Study. *Dalton Trans.* **2018**, *47*, 17153–17159. [[CrossRef](#)] [[PubMed](#)]



23. Arena, F.; Torre, T.; Raimondo, C.; Parmaliana, A. Structure and Redox Properties of Bulk and Supported Manganese Oxide Catalysts. *Phys. Chem. Chem. Phys.* **2001**, *3*, 1911–1917. [[CrossRef](#)]
24. Bulavchenko, O.A.; Konovalova, V.P.; Saraev, A.A.; Kremneva, A.M.; Rogov, V.A.; Gerasimov, E.Y.; Afonasenkov, T.N. The Catalytic Performance of CO Oxidation over MnOx-ZrO2 Catalysts: The Role of Synthetic Routes. *Catalysts* **2022**, *13*, 57. [[CrossRef](#)]
25. Di Castro, V.; Polzonetti, G. XPS Study of MnO Oxidation. *J. Electron. Spectrosc. Relat. Phenom.* **1989**, *48*, 117–123. [[CrossRef](#)]
26. Feng, X.; Cox, D.F. Na Deposition on MnO(100). *Surf. Sci.* **2016**, *645*, 23–29. [[CrossRef](#)]
27. Han, Y.-F.; Chen, F.; Zhong, Z.; Ramesh, K.; Chen, L.; Widjaja, E. Controlled Synthesis, Characterization, and Catalytic Properties of Mn<sub>2</sub>O<sub>3</sub> and Mn<sub>3</sub>O<sub>4</sub> Nanoparticles Supported on Mesoporous Silica SBA-15. *J. Phys. Chem. B* **2006**, *110*, 24450–24456. [[CrossRef](#)]
28. Ilton, E.S.; Post, J.E.; Heaney, P.J.; Ling, F.T.; Kerisit, S.N. XPS Determination of Mn Oxidation States in Mn (Hydr)Oxides. *Appl. Surf. Sci.* **2016**, *366*, 475–485. [[CrossRef](#)]
29. Murray, J.W.; Dillard, J.G.; Giovanoli, R.; Moers, H.; Stumm, W. Oxidation of Mn(II): Initial Mineralogy, Oxidation State and Ageing. *Geochim. Cosmochim. Acta* **1985**, *49*, 463–470. [[CrossRef](#)]
30. Biesinger, M.C.; Payne, B.P.; Grosvenor, A.P.; Lau, L.W.M.; Gerson, A.R.; Smart, R.S.C. Resolving Surface Chemical States in XPS Analysis of First Row Transition Metals, Oxides and Hydroxides: Cr, Mn, Fe, Co and Ni. *Appl. Surf. Sci.* **2011**, *257*, 2717–2730. [[CrossRef](#)]
31. Vaz, C.A.F.; Prabhakaran, D.; Altman, E.I.; Henrich, V.E. Experimental Study of the Interfacial Cobalt Oxide in Co<sub>3</sub>O<sub>4</sub>/α - Al<sub>2</sub>O<sub>3</sub> (0001) Epitaxial Films. *Phys. Rev. B* **2009**, *80*, 155457. [[CrossRef](#)]
32. Chuang, T.J.; Brundle, C.R.; Rice, D.W. Interpretation of the X-Ray Photoemission Spectra of Cobalt Oxides and Cobalt Oxide Surfaces. *Surf. Sci.* **1976**, *59*, 413–429. [[CrossRef](#)]
33. Lukashuk, L.; Föttinger, K.; Kolar, E.; Rameshan, C.; Teschner, D.; Hävecker, M.; Knop-Gericke, A.; Yigit, N.; Li, H.; McDermott, E.; et al. Operando XAS and NAP-XPS Studies of Preferential CO Oxidation on Co<sub>3</sub>O<sub>4</sub> and CeO<sub>2</sub>-Co<sub>3</sub>O<sub>4</sub> Catalysts. *J. Catal.* **2016**, *344*, 1–15. [[CrossRef](#)]
34. Liang, Y.; Wang, H.; Zhou, J.; Li, Y.; Wang, J.; Regier, T.; Dai, H. Covalent Hybrid of Spinel Manganese–Cobalt Oxide and Graphene as Advanced Oxygen Reduction Electrocatalysts. *J. Am. Chem. Soc.* **2012**, *134*, 3517–3523. [[CrossRef](#)] [[PubMed](#)]
35. Bordeneuve, H.; Tenailleau, C.; Guillemet-Fritsch, S.; Smith, R.; Suard, E.; Rousset, A. Structural Variations and Cation Distributions in Mn<sub>3-x</sub>Co<sub>x</sub>O<sub>4</sub> (0 ≤ x ≤ 3) Dense Ceramics Using Neutron Diffraction Data. *Solid. State Sci.* **2010**, *12*, 379–386. [[CrossRef](#)]
36. Mitran, G.; Chen, S.; Seo, D.-K. Role of Oxygen Vacancies and Mn<sup>4+</sup>/Mn<sup>3+</sup> Ratio in Oxidation and Dry Reforming over Cobalt-Manganese Spinel Oxides. *Mol. Catal.* **2020**, *483*, 110704. [[CrossRef](#)]
37. Omata, K.; Takada, T.; Kasahara, S.; Yamada, M. Active Site of Substituted Cobalt Spinel Oxide for Selective Oxidation of COH<sub>2</sub>. Part II. *Appl. Catal. A Gen.* **1996**, *146*, 255–267. [[CrossRef](#)]
38. Xie, X.; Li, Y.; Liu, Z.-Q.; Haruta, M.; Shen, W. Low-Temperature Oxidation of CO Catalysed by Co<sub>3</sub>O<sub>4</sub> Nanorods. *Nature* **2009**, *458*, 746–749. [[CrossRef](#)] [[PubMed](#)]
39. Ravel, B.; Newville, M. ATHENA, ARTEMIS, HEPHAESTUS: Data Analysis for X-Ray Absorption Spectroscopy Using IFEFFIT. *J. Synchrotron Rad.* **2005**, *12*, 537–541. [[CrossRef](#)]
40. Newville, M. EXAFS Analysis Using FEFF and FEFFIT. *J. Synchrotron Rad.* **2001**, *8*, 96–100. [[CrossRef](#)]
41. Scofield, J.H. Hartree-Slater Subshell Photoionization Cross-Sections at 1254 and 1487 eV. *J. Electron Spectrosc. Relat. Phenom.* **1976**, *8*, 129–137. [[CrossRef](#)]
42. Shirley, D.A. High-Resolution X-Ray Photoemission Spectrum of the Valence Bands of Gold. *Phys. Rev. B* **1972**, *5*, 4709–4714. [[CrossRef](#)]

**Disclaimer/Publisher’s Note:** The statements, opinions and data contained in all publications are solely those of the individual author(s) and contributor(s) and not of MDPI and/or the editor(s). MDPI and/or the editor(s) disclaim responsibility for any injury to people or property resulting from any ideas, methods, instructions or products referred to in the content.